Applied Surface Science 605 (2022) 154742

Contents lists available at ScienceDirect

Applied Surface Science

journal homepage: www.elsevier.com/locate/apsusc

Full Length Article

Shape-controlled monolayer $MoSe_2$ flakes by chemical vapor deposition towards tuning the photoluminescence emission

C. González [a,b], J.P.B. Silva [c,*], A.S. Viana [d], K. Gwozdz [e], O. Conde [a,b,*]

[a] Departamento de Física, Faculdade de Ciências, Universidade de Lisboa, 1749-016 Lisboa, Portugal
[b] CeFEMA-Center of Physics and Engineering of Advanced Materials (Assoc. Laboratory of Physics for Materials and Emergent Technologies, LaPMET), Universidade de Lisboa, 1749-016 Lisboa, Portugal
[c] CF-UM-UP–Physics Centre of Minho and Porto Universities (Assoc. Laboratory of Physics for Materials and Emergent Technologies, LaPMET), University of Minho, Campus de Gualtar, 4710-057 Braga, Portugal
[d] Centro de Química Estrutural, Institute of Molecular Sciences, Departamento de Química e Bioquímica, Faculdade de Ciências, Universidade de Lisboa, 1749-016 Lisboa, Portugal
[e] Department of Quantum Technologies, Faculty of Fundamental Problems of Technology, Wroclaw University of Science and Technology, Wroclaw 50-370, Poland

ARTICLE INFO

Keywords:
Transition metal dichalcogenides
Chemical vapor deposition
$MoSe_2$ monolayer
Morphology control

ABSTRACT

In this study, we report on the controllable chemical vapor deposition (CVD) synthesis of monolayer $MoSe_2$ flakes with different shapes such as hexagons, triangles, sawtooth hexagons, dendrites and fractals deposited on SiO_2/Si substrates. This broad range of morphologies is due to the change in the vapor composition resulting from the confinement of the MoO_3 and Se vapor and to the variation in the growth rate of the variable shaped $MoSe_2$ crystals. It is also revealed that the photoluminescence (PL) response of the $MoSe_2$ flakes is strongly affected by their shape and size. Our findings will open new avenues towards achieving morphology-controlled monolayer $MoSe_2$ flakes for optoelectronic and energy harvesting systems.

1. Introduction

2D transition metal dichalcogenides (TMDs) with chemical formula MX_2 (M = Mo, W and X = S, Se) [1,2] have promising properties due to their electronic characteristics, their sizable bandgap around 1–2 eV [3], high spin–orbit coupling [1,4,5] and non-zero Berry curvature [6]. Furthermore, the direct electronic transition that occurs in the monolayers related to quantum and dielectric confinement [7], rather than the indirect electronic transition that occurs in the bulk [8–10], promotes the integration of these groundbreaking layered materials into ultra-thin field effect transistors (FETs) [11–15] with a high on/off current ratio and lower response time, ultrasensitive photodetectors [16,17], photovoltaic cells [18] and catalytic applications [19,20]. This versatility of applications even includes the combination of TMDs with different materials such as ferroelectrics, creating novel heterostructures [21,22] that are the building blocks of electronic and optoelectronic devices.

Within the TMDs materials, $MoSe_2$ has been less studied than MoS_2 due to the higher chemical reactivity and lower vaporization temperature of S compared to Se [23]. However, the strong light–matter interaction of $MoSe_2$ and its direct bandgap close to that of silicon (1.5 eV), supported by a high intensity photoluminescence (PL) effect, make it a preferred material for solar spectrum-related applications [17].

Among all the methods used to grow TMDs [24–31], the CVD technique has the highest yield at the lowest cost, guaranteeing the crystalline quality required by the many applications. The morphologies of the CVD grown mono-to-few layer $MoSe_2$ flakes comprise triangles, triangles with truncated vertices, hexagons, sawtooth hexagons, fractals, etc [32]. However, it is not clear if all the different shaped MoSe2 flakes are monolayers. Usually, monolayer triangular flakes display a reduced number of defects due to their equilibrium configuration [33] and thus, are the preferred ones for optoelectronic applications. On the contrary, sawtooth morphologies and fractals are important for (photo)catalytic applications due to the high number of active sites [34]. Therefore, in order to achieve monolayer growth with a given morphology and large size, the growth parameters should be finely tuned. Moreover, also the control of the PL response is relevant for the light-based applications.

Here, we report the CVD growth of single and few-layer $MoSe_2$ with different domain shapes onto SiO_2/Si substrates. The optimization of experimental conditions allows the application of these materials in

* Corresponding authors.
E-mail addresses: josesilva@fisica.uminho.pt (J.P.B. Silva), omconde@ciencias.ulisboa.pt (O. Conde).

https://doi.org/10.1016/j.apsusc.2022.154742
Received 22 April 2022; Received in revised form 29 August 2022; Accepted 30 August 2022
Available online 3 September 2022

innovative projects, being a model of the interdependence between the main characteristics of the system: the experimental parametric properties, the morphology characteristics and the PL response.

2. Experimental details

To synthetize $MoSe_2$ monolayer domains, atmospheric pressure chemical vapor deposition technique (APCVD) was used because, in other TMDs, it was shown to give rise to domains with larger lateral size than low-pressure chemical vapor deposition (LPCVD) [5]. The APCVD experimental set up shown in Fig. S1 consists of a 1-meter-long quartz tube closed at its ends by flanges with passages for the gases inlet and outlet, inserted in a two-zone temperature controlled tubular furnace [35].

MoO_3 (Neyco, 99.99 % purity) and Se (Alfa Aesar, 99.999 % purity) powder precursors were employed; they were placed in quartz boats, inside the quartz tube, located at positions where the furnace temperature is 820 °C and 292 °C, respectively. Although several substrates have been used in the synthesis of transition metal dichalcogenides, such as silicon [17], sapphire [36,37], mica [17] and glass [38,39], 300 nm SiO_2/Si substrates were used since they provide greater contrast of the $MoSe_2$ flakes when observed by optical microscopy [23]. The substrates were also placed over quartz boats, next to the MoO_3 powder (Fig. S1), with the oxide surface facing down. Prior to their insertion in the APCVD reactor, the substrates were cleaned with acetone (>99.5 % purity) and isopropanol (≥ 99.5 % purity).

Before reaction, the quartz tube was flushed with 200 sccm of Argon for two hours at room temperature, ensuring that no secondary chemical reactions involving oxygen and, consequently, no contamination of the samples occur. During the growth at high temperature a mixture of Ar and H_2 at variable fluxes entered the tube from upstream side. The MoO_3 precursor is converted to MoO_{3-x} by the H_2 acting as reducing gas, an indispensable condition for the growth of $MoSe_2$ monolayers [18,40]. In the first 10 min after growth, an Ar flow of 10 sccm was applied and afterwards the furnace cooled down to room temperature naturally.

The mass of MoO_3 (0.08 g) was kept constant in all experiments, while the effect that a variation in the mass of Se (0.32 g and 0.60 g) caused on the layers morphology was studied. The distance between the precursor holders (19.6 cm) was kept constant throughout the experiments. Table S1 shows the experimental parameters used for preparing the $MoSe_2$ samples.

The surface morphology of the samples was analyzed by optical microscopy, scanning electron microscopy (SEM, Hitachi SEM S2400) and atomic force microscopy (AFM, Multimode 8HR coupled to a Nanoscope V, Digital Instruments, Bruker) in tapping mode, using RTESP 300 probes with a resonance frequency of ca. 300 kHz (Bruker). Raman spectroscopy (Horiba, LabRam HR800 Evolution system) and PL measurements (T64000 Horiba monochromator) were performed to evaluate the quality of the samples. Both spectroscopic techniques used an excitation wavelength of 532 nm.

3. Results and discussion

The CVD technique, although experimentally simple, is parametrically complex. Factors such as the temperature of the precursors, the total flow rate (Ar + H_2), the hydrogen concentration, the growth time, the mass of the precursors and the distance between them, and the substrate configuration have a strong impact on the morphology, lateral size and nucleation density of the deposited structures. In this work, we prepared several samples while varying one deposition parameter at a time (Table S1), in order to make comparisons possible.

3.1. Morphological study

Firstly, we analyzed the influence of the total flow rate, Φ_T, from 30 sccm to 200 sccm, on the morphology of the $MoSe_2$ flakes. For the lowest value, Φ_T = 30 sccm (sample 1), only rhombuses were found on the substrate surface. The Raman spectrum of this sample could be assigned to MoO_2 and Mo_4O_{11} [41,42], indicating an incomplete selenization of MoO_{3-x} probably due to the lack of Se supply because of the low flow rate of the carrier gas.

Fig. 1 shows the SEM micrographs of samples 2–7. A higher flow rate of 50 sccm (Fig. 1a) produces hexagons with lateral sizes between 0.8 and 2.8 μm and truncated-vertices triangles with lateral sizes between 0.5 and 3.9 μm, both occupying a surface area of 28.3 %. Previously, it has been shown that the hexagonal structure corresponds to a ratio of the Mo:Se atoms of 1/2. If the ratio is less than this value, triangles with Se-zz edges are synthesized due to the Mo-zz edges growing faster. Otherwise, triangles with Mo-zz edges will form [33]. The hexagonal morphology was previously obtained by changing the concentration of hydrogen [13] and by varying the temperature of the warmest zone in the furnace [43]. In our study, it is found that a change of the flow rate in the domain of low fluxes also causes an equal rate of growth of the Mo-zz and Se-zz edges thus, the formation of hexagonal morphology.

In samples 3 and 4, Φ_T = 60 sccm and 70 sccm (Fig. 1b-c), equilateral triangles were obtained. In sample 3, the $MoSe_2$ synthesis occupies 40.9 % of the substrate surface area and the mean triangular lateral size is 2.8 μm with the maximum size being 7.25 μm, while in sample 4 the nucleation density decreases and the lateral size increases, with triangles reaching 14 μm. Thus, the role of total flow rate is not just to expand the lateral size of the triangle, but also to suppress the development of sawtooth shapes, both triangles and hexagons. Nevertheless, according to Fig. 1d, an increase of the total flow rate to 80 sccm (sample 5) leads to a decrease of the mean lateral size to 0.86 μm and the larger isolated triangle of the figure reaches about 12.8 μm. The AFM images of sample 5 (Fig. 1g-i) reveal a triangle with an additional vertex, a six-point star, and an isolated domain with several vertices. All isolated flakes have height profiles taken along lines 1–3 on the AFM images that agree with those reported for $MoSe_2$ monolayers [18]. Furthermore, the AFM images display a reliable data pattern: all domains have nanoparticles between the vertices. From the observed results, we deduced that the nanoparticles are the barriers that encircle the monolayers, preventing the increase in triangular lateral growth. In previous observations [21,44], it was assumed that these are Se nanoparticles. Although we could not find the phase diagram of the Mo–Se system in the literature, given the chemical similarity between the selenium and sulphur species we can use the Mo–S phase diagram [45] to explain the presence of the Se nanoparticles and thus, corroborate the previous assumptions. When there is excess of Se in the gas phase, upon cooling there is formation of solid $MoSe_2$ and liquid Se that can be segregated to the edges of the solid domains by diffusion. Upon further cooling, the Se nanoparticles can solidify or continue to diffuse along the boundary, coalescing into even larger nanoparticles that solidify between the vertices. This would explain the existence of nanoparticles accumulated on the edges of triangles.

In contrast, from 100 sccm (sample 6) onwards the morphological dynamics completely changes. Triangles with sharper vertices, called three-point star, are visualized on the SEM micrograph of Fig. 1e. In related work for MoS_2 [3], the three-point stars were synthesized when the Mo-zz edges grow at least three times faster than the S-zz edges in the primordial hexagonal nuclei. Extrapolating these findings to $MoSe_2$, this confirms the presence of a Se-saturated atmosphere due to the increased flux that carries more Se to the substrate. For Φ_T = 200 sccm (Fig. 1f, sample 7), the fractal behavior without self-similarity predominates, although some dendritic domains were also observed. Some of the fractals resemble triangles but with fractal-like edges and interstices in the middle of the isolated domains.

The growth kinetics is also dependent on the content of hydrogen in the gas phase. To study the contribution of the reducing gas to the size modification, a constant flow rate was maintained, which could be low (Φ_T = 50 sccm), medium (Φ_T = 70 sccm), or high (Φ_T = 200 sccm). For 50 sccm, samples 2 (15 %H_2) and 8 (10 %H_2) have well-developed

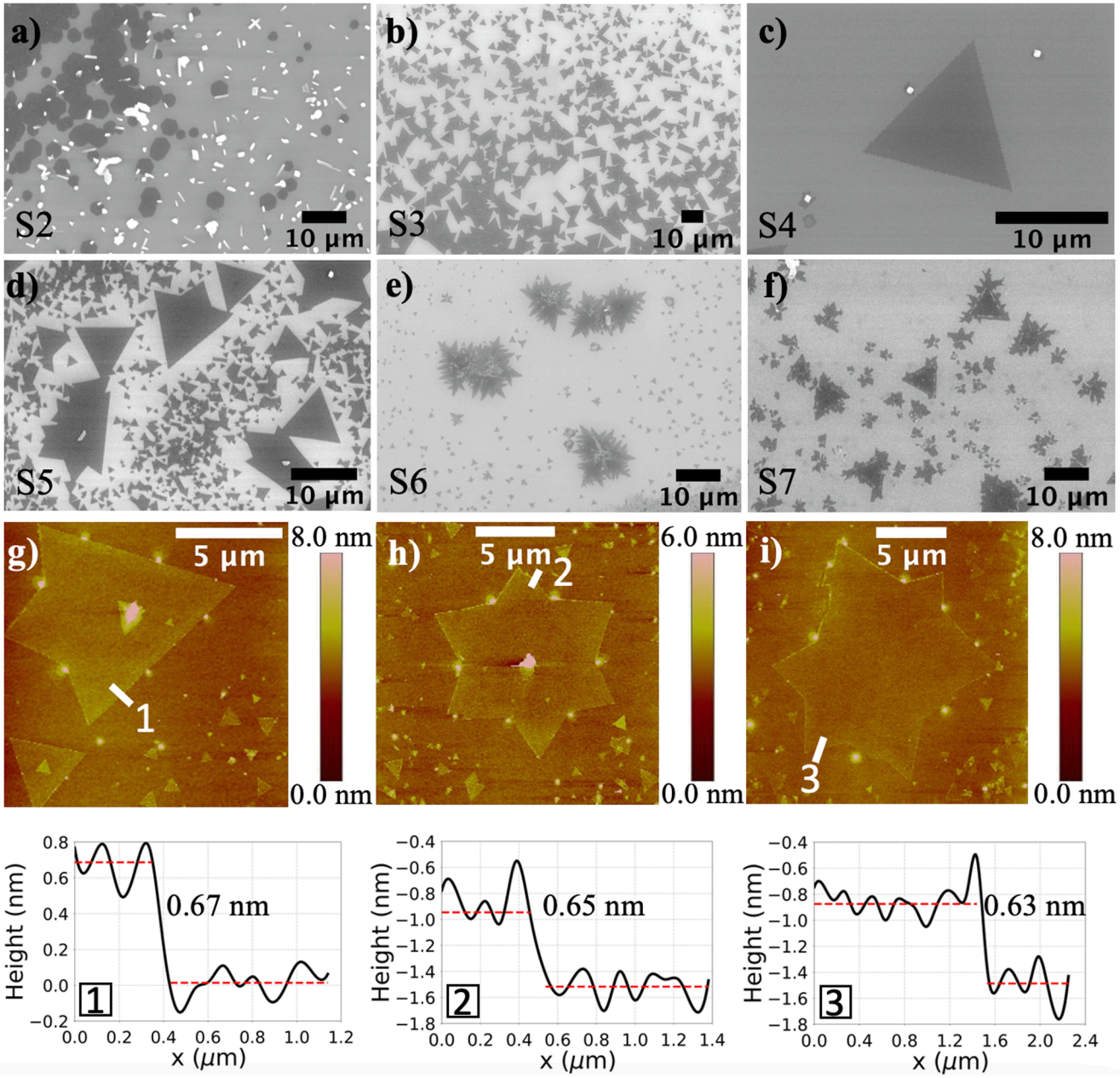

Fig. 1. (a-f) SEM micrographs of $MoSe_2$ microstructures for a total flow rate of: (a) 50 sccm, (b) 60 sccm, (c) 70 sccm, (d) 80 sccm, (e) 100 sccm and (f) 200 sccm, corresponding to samples 2–7, respectively. (g-i) AFM images of sample 5: (g) a triangle with an additional vertex, (h) a six-point star and (i) an isolated domain with several vertices. Height profiles, taken along lines 1–3 on the AFM images are shown in the bottom panel.

hexagonal flakes, as shown on the SEM images (Figs. 1a and 2a). Only a hexagon with a lateral size of 14 μm was obtained in sample 8 while the maximum hexagonal edge is 2.8 μm for sample 2. Therefore, for the lower fluxes, by increasing the $\%H_2$, although the hexagonal morphology is conserved, there is an increase in nucleation density and, concomitantly, a decrease in lateral size.

For 70 sccm and keeping the deposition time of 15 min, the percentage of H_2 was changed from 10 % to 20 % (Fig. 2b-f). For 10 % H_2 (sample 9) and 12.5 % H_2 (sample 10), small triangles with a high nucleation density are distributed on the substrate surface, giving rise to monolayers whose lateral size may reach up to $\approx$ 40 μm. This was the largest lateral size obtained in this work for perfectly triangular monolayers, whose height was checked by AFM to be 0.69 nm, although domains with additional vertices and dimension greater than 40 μm were also synthesized. At a relative percentage of hydrogen of 17.5 % and 20 % (samples 11 and 12), the triangular domains become more complex resulting in sawtooth hexagons.

Similarly, for the same total flow rate (ϕ = 70sccm) with a deposition time of 10 min, the concentration of hydrogen was changed from 10 % to 17.5 %, as can be observed in Fig. 3a-c. As the concentration of H_2 increases, the triangular mean lateral size also increases in different proportions. From 10 % to 15 % H_2, triangular mean lateral size increases 5.0 % while from 15 % to 17.5 % H_2 an increase of 153.6 % can be seen. A slight variation in the hydrogen concentration in the tubular atmosphere prompts to a more optimal reduction of MoO_3 to MoO_{3-x}. Additionally, the number of layers of the triangles in samples 14 and 15 was determined by AFM (Fig. 3d-e). The height profiles of 0.69 nm and 0.71 nm obtained in the triangles with a lateral size of 9.05 μm (sample 14) and 8.57 μm (sample 15), respectively, confirm the presence of monolayers. It should be noted that in accordance with our previous results,

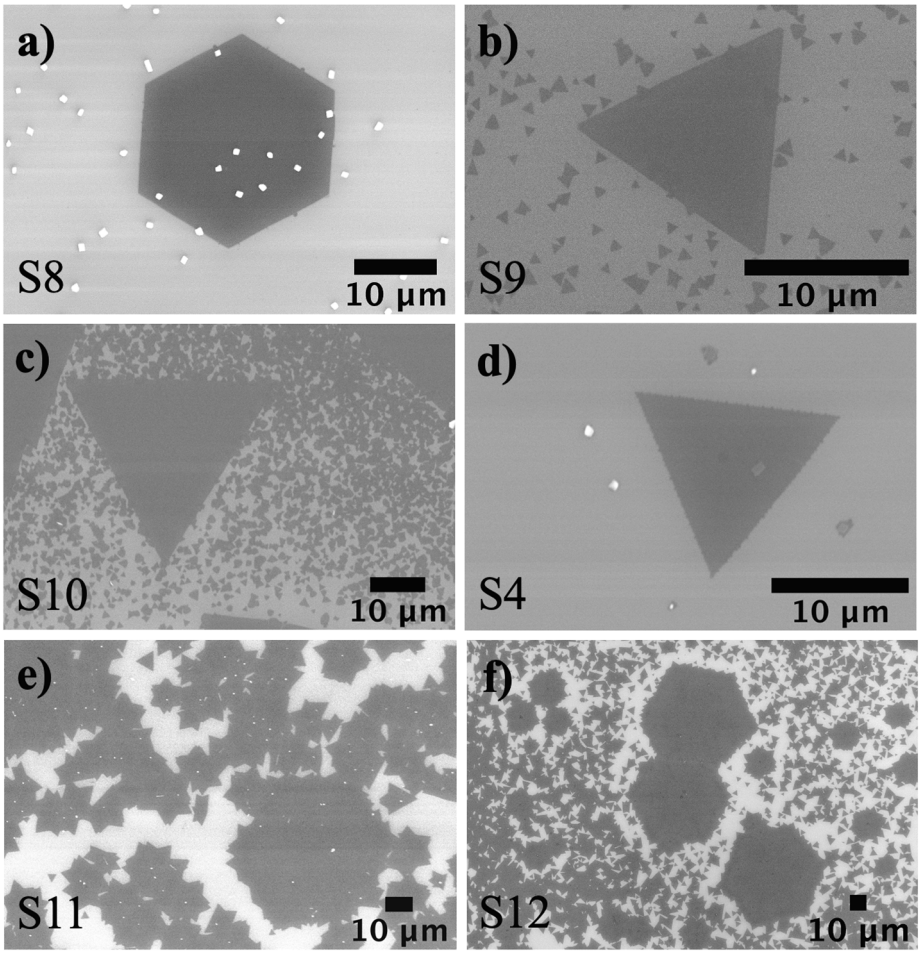

Fig. 2. SEM micrographs of $MoSe_2$ domains for total flow rate of 50 sccm (a) and 70 sccm (b-f). The hydrogen relative percentages are: (a) 10% (sample 8), (b) 10% (sample 9), (c) 12.5% (sample 10), (d) 15% (sample 4), (e) 17.5% (sample 11) and (f) 20% (sample 12).

some triangles are limited by nanoparticles, as seen on the AFM image of sample 14. Nanoparticles, with a structure identical to fullerenes, located in the center of some domains were analyzed in previous studies [46,47] for MoS_2, and it was concluded that they were constituted by $MoO_{3-x}S_y$, which after the sulfurization process acted as nuclei for the growth of multilayer MoS_2. In our samples, the nanoparticles appear on top and at the boundaries of the monolayer domains, instead of in the multilayer flakes, and should be constituted just of Se, as explained above.

Thereafter, the total flow rate was increased to 200 sccm for a deposition time of 15 min and a relative percentage of hydrogen of 10 % (sample 16) and 15 % (sample 7). The SEM images of Fig. 4a-c illustrate diverse morphologies, where sample 16 displays rounded vertices and sample 7 contains fractal structures. An increase in the total flux and the relative percentage of H_2 is not a sufficient condition for the growth of the domains, maintaining the triangular shape. With increased mass transport, molecules have less time to diffuse to more thermodynamically stable positions.

Moreover, the supply of precursors is one of the most significant deposition parameters, as it determines the amount of material available for the synthesis and, therefore, the Mo:Se ratio. All samples, apart from sample 17 (Fig. 4c), maintained a constant mass of, approximately, 0.6 g for Se and 0.08 g for MoO_3. Sample 17 had the same MoO_3 mass as other samples, while Se mass was reduced to ~ ½ and the maximum total flow rate (200 sccm) with 15 % H_2 was used. The development of fractal domains without self-similarity predominate in image 4b, while sample 17 shows that dendritic domains were synthesized. The fractals in sample 7 follow the diffusion-limited aggregation (DLA) growth model [48], introduced by Witten and Sander [49] in 1981.

In contrast to an irregular morphology, dendrites with a high nucleation density are represented in Fig. 4c. Dendrites are formed by atoms that diffuse along preferential directions forming the “branches” of the structure. Most of the dendritic structures in the SEM image have the three crystallographic directions of a snowflake. However, larger dendrites have more than six self-similar branches. In these structures there was practically no coalescence: neighboring atoms introduce an anisotropy and as dendrites only grow in lower energy directions, the growth of that branch is suppressed. P.Wang *et al.* [48] suggested a model based on nucleation, diffusion-limited aggregation of atoms to neighboring nuclei and atoms, and relaxation of the aggregate structure, the latter phase resulting from the temperature decrease. They concluded that for high sticking coefficients, the fractal exhibits strong dendritic characteristics with a smaller fractal dimension (Minkowski-Bouligand dimension [50]).

There are two mechanisms that participate in the diffusion process: the diffusion of atoms on the surface of the substrate until they reach the lateral surface of a crystal, and the diffusion of atoms already aggregated at the edges of the crystal, to fix themselves in thermodynamic positions. Other studies concluded that the dominant morphology was fractal at low temperatures since diffusion along the substrate surface dominates rather than edge diffusion [32]. For a higher MoO_3 vaporization rate, more atoms reach the substrate and the predominant form is dendritic [20]. Sample 7, with a high total flow rate, has a greater mass of Se that participates in the chemical conversion. At the end of the growth time,

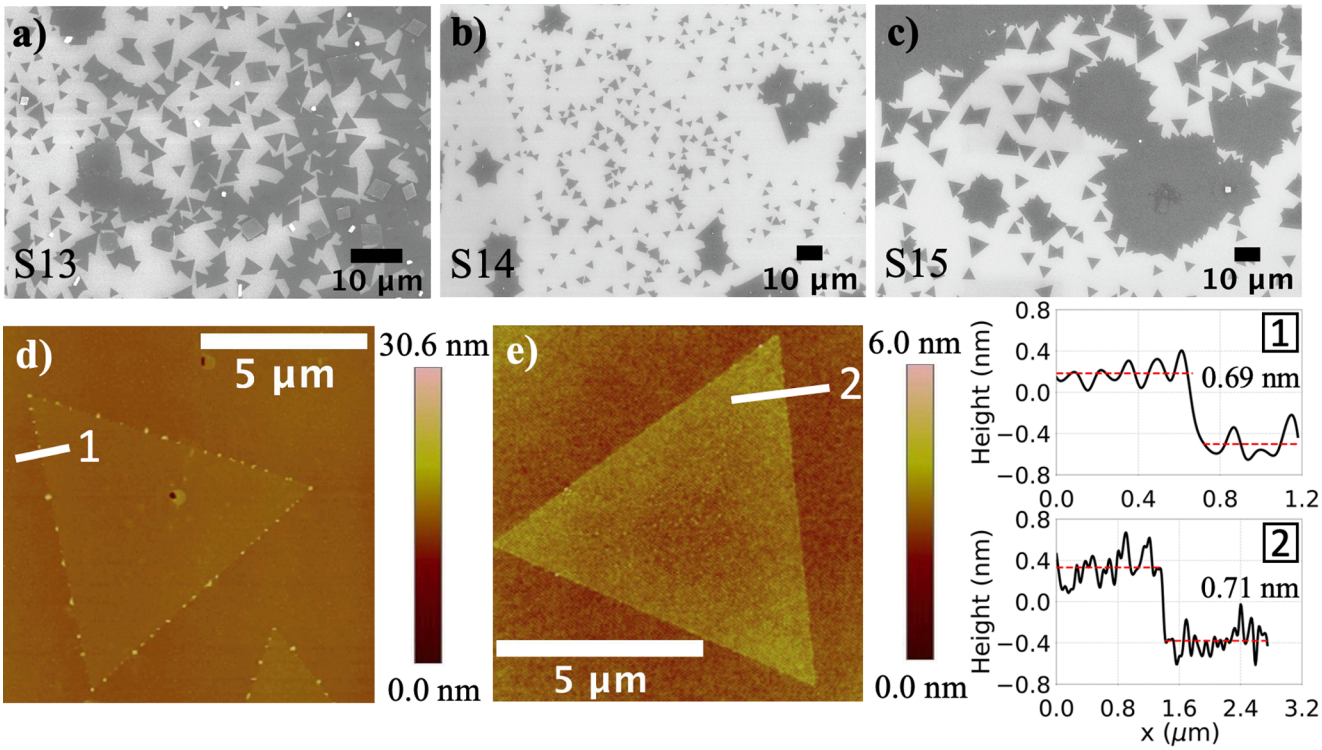

Fig. 3. SEM micrographs of $MoSe_2$ flakes for total flow rate of 70 sccm, deposition time of 10 min and hydrogen relative percentage of: (a) 10%, (b) 15% and (c) 17.5%, corresponding to samples 13–15, respectively. (d-e) AFM images of samples 14 and 15. The height profiles, taken along lines 1 and 2 in the AFM images, are shown on the right panel.

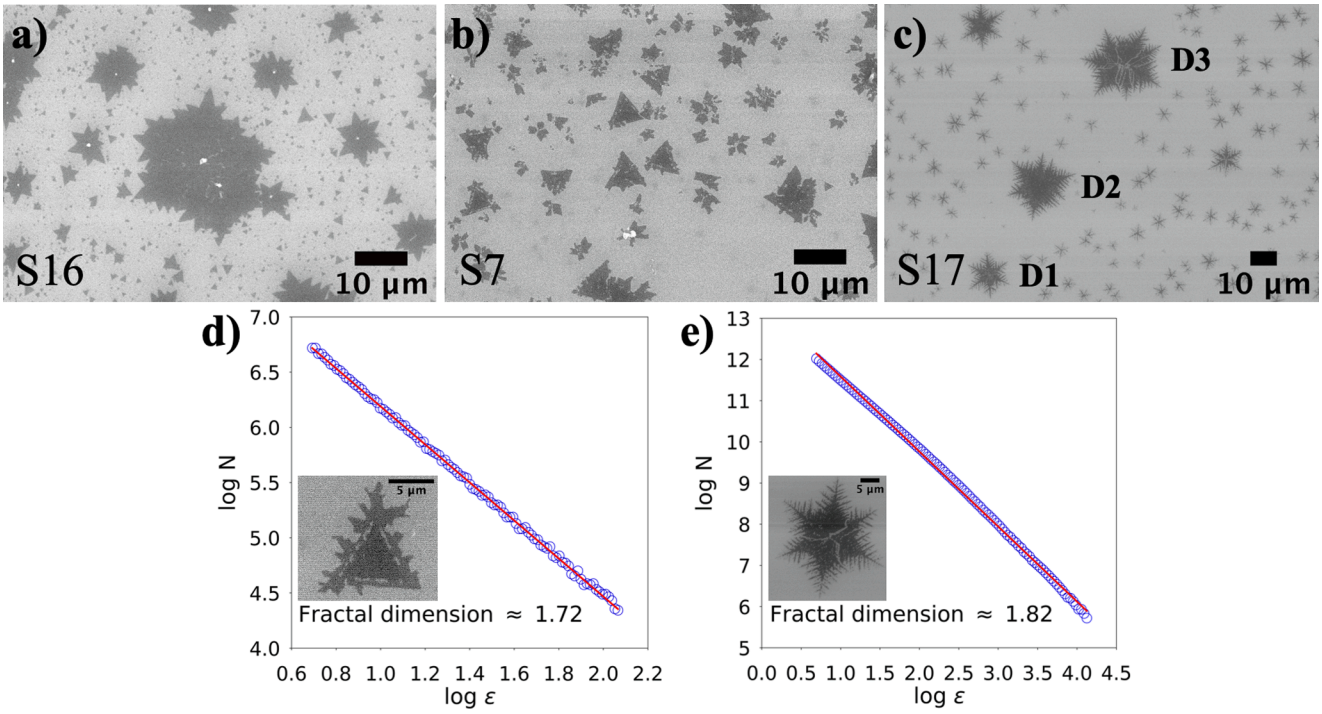

Fig. 4. SEM micrographs of the CVD-grown crystals on SiO_2/Si substrates for total flow rate of 200 sccm and hydrogen relative percentage of: (a) 10 % (sample 16) and (b) 15 % (sample 7). (c) Sample 17 has the same experimental parameters as sample 7 but a smaller m(Se)/m(MoO_3) ratio as indicated on the figure. The size of the dendrites D1, D2 and D3 are 14.7, 23.6 and 26.5 μm, respectively. The fractal dimensions of samples 7 (d) and 17 (e) were calculated using the box-counting method.

there will be a gaseous atmosphere very rich in Se and Mo. As the cooling rate is fast at the beginning, just after the growth time, the atoms will tend to deposit in a disorderly way on previous nucleation sites or give rise to new nucleation points on the substrate (secondary nucleation), as it occurs in sample 7, which would justify the existence of fractals around some triangle-like structures.

However, in sample 17, a decrease in Se mass causes a higher partial concentration of MoO_3 vapor, which justifies a high nucleation density. As Mo atoms are heavier than Se atoms, Mo atoms spend longer traveling on the substrate [32], increasing the probability of nucleation. As the Se/Mo ratio is lower in sample 17 (4) than in sample 7 (7.5), the smaller amount of Se atoms bond covalently to the Mo atoms found on the substrate, forming more organized domains.

As the total flow rate is high, mass transport is more favorable than diffusion along the surface of the substrate [23], so atoms deposit within a very limited time to rearrange themselves. Atoms that deposit at the beginning of the growth time have more time to rearrange themselves, forming larger domains, than atoms that deposit closer to the end of the growth time. This justifies the existence of large fractal hexagons with many rounded edges in sample 7, where fractal triangles and small fractals meet around, with a high nucleation density, and justifies the existence of dendrites with more than six branches in sample 17. The largest dendrites in sample 17 have a larger central region than the smaller six-branch dendrites that are distributed around the larger dendrites. Larger dendrites have a lower nucleation density than smaller dendrites and a larger central zone, as mentioned above, so these nucleation centers were the first to be formed and the atoms had more time to rearrange themselves and aggregate to the center of the dendrite, enabling the creation of a greater number of branches, contributing to the growth of the structure.

The box-counting method was applied to calculate the dimension of some representative fractals of samples 7 and 17, adapting a program from the University of Toronto [51]. The fractal dimension is given by the slope of the following linearization [48]:

$$\log(N(\varepsilon)) = -D\log(\varepsilon) + \log(k)$$

where ε is the side length of the boxes, k is a proportionality constant and $N(\varepsilon)$ is the number of boxes to cover the fractal. The fractal dimensions obtained for the SEM images in Fig. 4d and 4e were 1.72 and 1.82, respectively, corroborating the fractal dimensions in the literature [32,48].

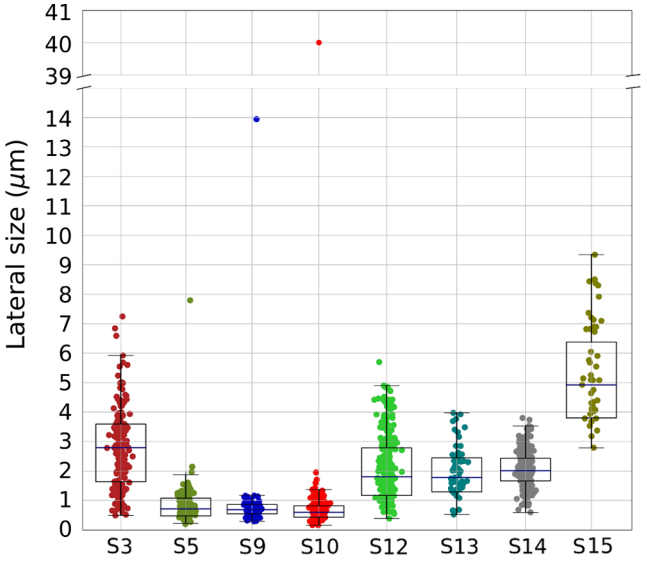

Fig. 5. Lateral size box plots of triangular monolayers that allow comparative analysis of data heterogeneity. Sample 4 was not included despite having large triangles due to its low density of triangular nucleation.

Variability, heterogeneity and distribution patterns of the experimental data related to triangular $MoSe_2$ domains were analyzed by box plots with a lognormal distribution (Fig. 5). The number of points in the box plots, the mean, the minimum and the maximum lateral size of the triangles are given in the supporting information (Table S2). Thus, for our experimental setup, the appropriate deposition conditions to reach the maximum triangular lateral size are an intermediate total flow rate ($\Phi_T = 70$ sccm), a growth time of 15 min and a hydrogen concentration of 10 % or 12.5 % (samples 9 and 10). In addition, sample 15 has the highest mean lateral size of all samples and sample 9 has the highest nucleation density (0.177 triangles μm^{-2}).

3.2. Raman microprobe analysis

In addition to the previous techniques, the analysis by micro-Raman spectroscopy constitutes a structural fingerprint for the identification of the $MoSe_2$ phase and allows getting a support of the number of layers measured by AFM. Raman spectra recorded at the center of different monolayer flakes, as determined by AFM, such as a triangular flake, a hexagon, and a small and a large fractal, revealed that they are all very similar in what regards to the Raman peaks that are present and their wave numbers. Fig. 6a-b displays the Raman spectra of a triangular monolayer and monolayer dendrite D3, respectively.

In general, the E_{1g}, A_{1g}, E^2_{2g} and E^1_{2g} phonon modes of low dimensional $MoSe_2$ can be observed. In particular, the out-of-plane A_{1g} vibration mode of the Se atoms [17] and the in-plane E^1_{2g} vibration mode of the Mo and Se atoms located close to 241 and 287 cm^{-1}, respectively, have been assigned to monolayer $MoSe_2$ [52–54], along with a value of 46 ± 1 cm^{-1} for the difference $\Delta(E^1_{2g} - A^1_g)$ [17,52,53]. In our case, the Raman shifts of the A_{1g}/E^1_{2g} modes measured, for instance, for the triangular flake of sample 9 and the small (D1) and large (D3) dendrites of sample 17 were, respectively, 239.2/285.7 cm^{-1}, 240.3/285.7 cm^{-1}

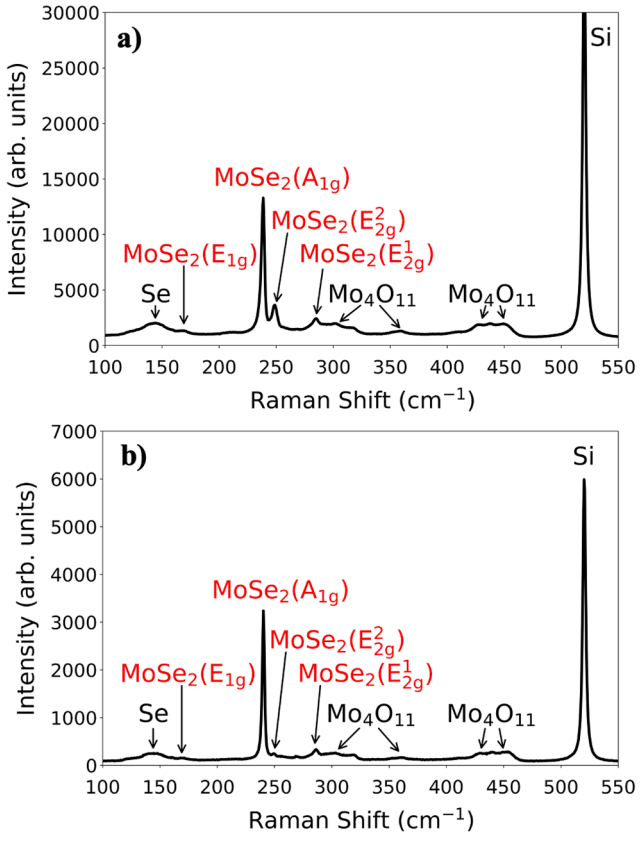

Fig. 6. Raman spectra of (a) a triangular monolayer and (b) monolayer dendrite D3.

and 240.3/286.2 cm^{-1}, with the differences being 46.5, 45.5 and 45.9 cm^{-1}. The set of these values clearly indicates that we are dealing with $MoSe_2$ monolayers. Furthermore, importantly is the absence of the B^1_{2g} vibration mode at 353 cm^{-1} for the three samples here mentioned, which confirms the intrinsic properties of the monolayers [53]. In addition, Fig. 6 shows other peaks that can be attributed to Se [55] and Mo_4O_{11} [42].

Therefore, regardless of whether the morphology is triangular or hexagonal or fractal, all the structures reveal monolayer behavior, which supports that for the experimental conditions utilized for preparing these samples domains grow preferentially laterally, being limited at the vertices by nanoparticles, instead of growing vertically where bilayers and multilayers would be formed.

3.3. Photoluminescence properties

The PL properties are strongly affected by the shape and size of the $MoSe_2$ flakes. Fig. 7a shows the PL spectra of triangular $MoSe_2$ flakes corresponding to samples 2, 3 and 9 with different lateral sizes of 2.8, 7.25 and 40 μm, respectively. It is possible to observe a dominant PL peak, which is the A-exciton (ground state exciton contribution), at 812 nm (1.527 eV) in the samples 2 and 3, while this PL peak is slightly shifted to 816 nm (1.519 eV) in sample 9. Regarding the PL peak intensity, it can be seen that it increases with the size of the triangles. Moreover, a second smaller peak is present at ~90 nm below (i.e. at ~200 meV higher energy), which corresponds to the B-exciton (higher spin–orbit split state) [56]. The ratio of the intensities of the A and B peak emissions is usually connected to the defect density in the samples [57]. To quantify the contribution of the B-emission feature to the PL spectra, we followed the procedure of K.M. McCreary *et al.* [58]. Fig. 7b shows the B-emission intensity and the B/A ratio as a function of A-emission intensity. It is possible to observe that the B-emission intensity increases with A-emission, while the B/A ratio tends to decrease with the increasing in the A-emission intensity, similarly to what was observed in other TMDs flakes [58], providing a qualitative measure of the sample quality.

The PL response of $MoSe_2$ monolayers with fractal shape was also investigated. The PL response at the center of the dendrites marked in Fig. 4c as D1, D2 and D3 is shown in Fig. 8a. It is possible to observe the presence of the A- and B-emissions. Moreover, the intensity of the dominant peak increases with the increase of the dendrites' size, while the PL peak position remains unchanged at 807 nm (1.536 eV). The B-emission intensity and the B/A ratio as a function of A-emission intensity is shown in Fig. 8b. As can be seen the B-emission intensity increases with A-emission intensity, while B/A decreases with A-emission intensity, thus suggesting that increasing the fractal size causes the decrease of the defect density. To understand this effect, PL spectra were recorded on two more places far from the center of the dendrite D3 (see Fig. S2 in the supporting information). As can be seen all the three PL spectra have their maximum intensity at the same wavelength, which is the characteristic one of $MoSe_2$ monolayers. Nevertheless, it can also be concluded that more defects should be present in the edges of the dendritic flake, responsible by the quite strong decrease of the PL intensity observed near the edges. A similar behavior was recently reported for dendritic MoS_2 flakes [59].

Fig. 9 illustrates a comparative analysis of the best $MoSe_2$ monolayers with different shapes in terms of the PL response. Therefore, Fig. 9a shows the PL response of a triangle, a dendrite and a hexagon of monolayer $MoSe_2$, from samples 9, 17 and 2, respectively. Both A- and B-emissions are present in all samples. The intensity of the A-peak emission is higher in the triangle and comparable in the dendrite and the

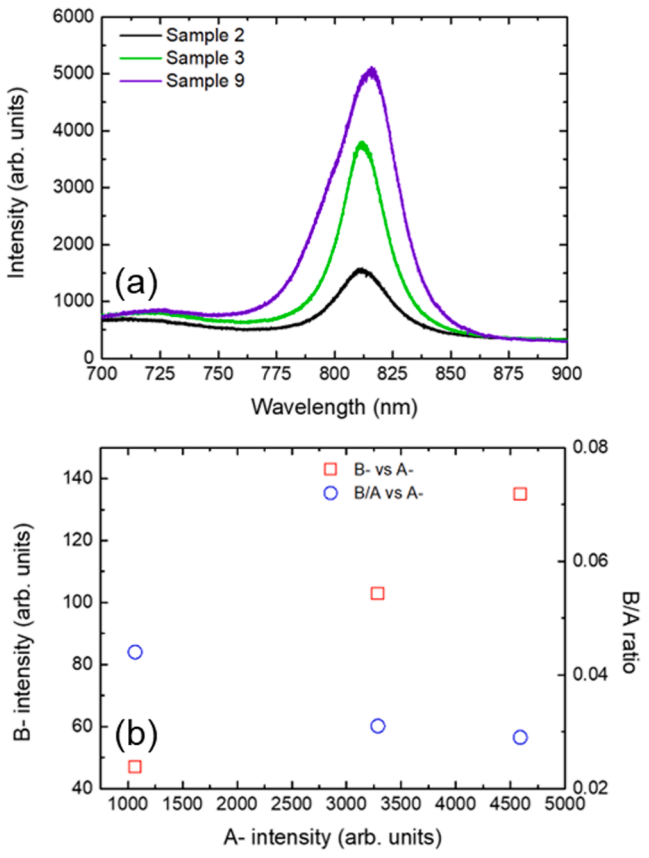

Fig. 7. (a) PL spectra and (b) B-intensity and B/A ratio as a function of A-intensity for monolayer $MoSe_2$ triangles of different size from samples 2, 3 and 9.

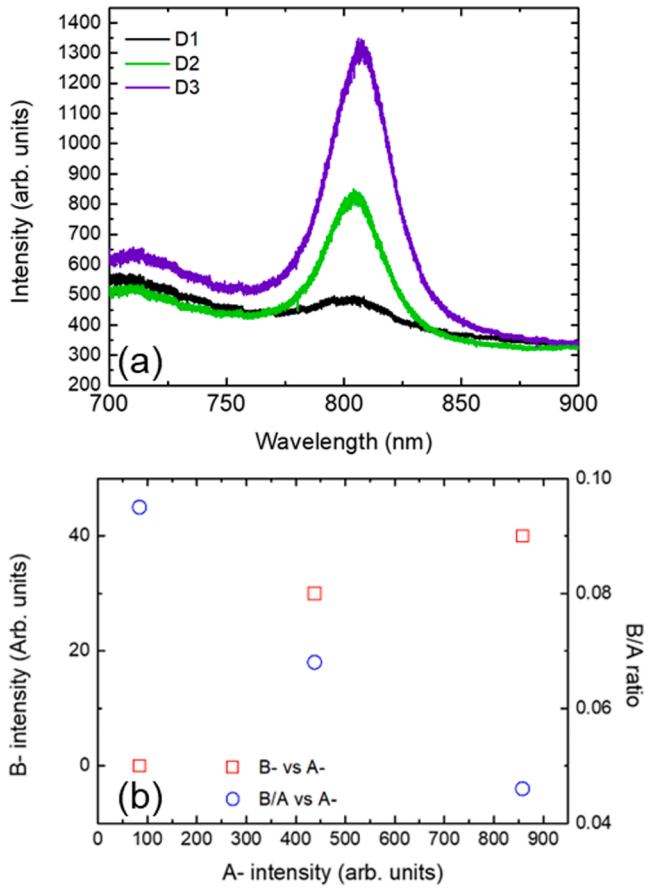

Fig. 8. (a) PL spectra and (b) B-intensity and B/A ratio as a function of A-intensity for the dendrites with different sizes.

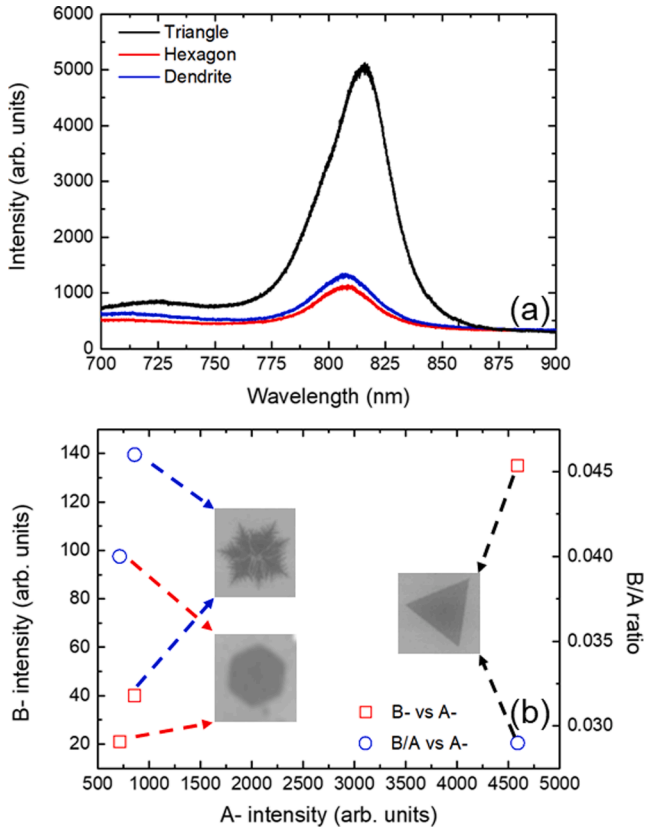

Fig. 9. (a) PL spectra and (b) B-intensity and B/A ratio as a function of A-intensity for monolayer $MoSe_2$ hexagon, triangle and dendrite from samples 2, 9 and 17, respectively.

hexagon. Contrary to the investigation of V. Singh *et al.* [41], who could not find PL emission close to the 800 nm from hexagonal shaped domains, the hexagon in Fig. 9a shows an A-peak emission at 807 nm, similarly to the one observed in the fractal. The B-emission intensity and the B/A ratio as a function of A-emission intensity are shown in Fig. 9b. It is possible to conclude that $MoSe_2$ triangles have the lowest defect density when compared to fractals and hexagons.

Therefore, this work provides an in-depth knowledge of the growth mechanisms of large-scale atomically thin $MoSe_2$ material via CVD and allows judicious selection of morphology to further fabricate high-quality $MoSe_2$ structures with improved optical response for optoelectronic devices.

4. Conclusions

In this work, $MoSe_2$ crystals were successfully synthesized by CVD onto SiO_2/Si substrates, using MoO_3 and Se powders as solid precursors. The relation between the experimental parameters and the formation of low-dimension $MoSe_2$ flakes with different shapes was established. It was revealed that the diffusion of atoms on the surface of the substrate and along the edges of the crystal, as well as the diffusion of atoms on the surface of the $MoSe_2$ monolayers is responsible for the different shapes. In addition, the characterization by SEM, AFM and Raman spectroscopy confirmed that the as-grown $MoSe_2$ is a monolayer, regardless of morphology. Moreover, a comprehensive study of the PL response of monolayer triangles, fractals and hexagons is provided, showing that the PL emission is higher in the case of triangular $MoSe_2$. Furthermore, $MoSe_2$ triangles have the lowest defect density when compared to fractals and hexagons.

In summary, this study reflects a comprehensive relation between the formation of low-dimension $MoSe_2$ layers with different shapes and their optical response. Our investigations also provide insight into morphological evolution during the CVD process that will prove to be beneficial when applied in devices fabrication.

Declaration of Competing Interest

The authors declare that they have no known competing financial interests or personal relationships that could have appeared to influence the work reported in this paper.

Data availability

Data will be made available on request.

Acknowledgments

This work was supported by the Portuguese Foundation for Science and Technology (FCT) in the framework of the Strategic Funding Contracts UIDB/04540/2020, UIDB/00100/2020 and UIDB/04650/2020. The author C. G. acknowledges a scholarship funded by the UIDB/04540/2020 contract. The author K. G. would like to thank the statutory grant (No. 8211104160) of Department of Quantum Technologies of Wroclaw University of Science and Technology.

Appendix A. Supplementary data

Supplementary data to this article can be found online at https://doi.org/10.1016/j.apsusc.2022.154742.

References

[1] S. Wang, G. Wang, X. Yang, H. Yang, M. Zhu, S. Zhang, G. Peng, Z. Li, Synthesis of monolayer $MoSe_2$ with controlled nucleation via reverse-flow chemical vapor deposition, Nanomaterials 10 (2019) 75, https://doi.org/10.3390/nano10010075.
[2] X. Wu, Y. Wang, P. Li, Z. Xiong, Research status of $MoSe_2$ and its composites: A review, Superlattices Microstruct. 139 (2020) 106388, https://doi.org/10.1016/j.spmi.2020.106388.
[3] S.Y. Yang, G.W. Shim, S.B. Seo, S.Y. Choi, Effective shape-controlled growth of monolayer MoS_2 flakes by powder-based chemical vapor deposition, Nano Res. 10 (2017) 255–262, https://doi.org/10.1007/s12274-016-1284-6.
[4] X. Lu, M. Utama, J. Lin, X. Gong, J. Zhang, Y. Zhao, S. Pantelides, J. Wang, Z. Dong, Z. Liu, W. Zhou, Q. Xiong, Large-area synthesis of monolayer and few-layer $MoSe_2$ films on SiO_2 substrates, Nano Lett. 14 (2014) 2419–2425, https://doi.org/10.1021/nl5000906.
[5] P. Liu, T. Luo, J. Xing, H. Xu, H. Hao, H. Liu, J. Dong, Large-Area WS_2 Film with Big Single Domains Grown by Chemical Vapor Deposition, Nanoscale Res. Lett. 12 (2017) 558, https://doi.org/10.1186/s11671-017-2329-9.
[6] B. Modtland, Exploring Valleytronics in 2D Transition Metal Dichalcogenides, PhD Thesis, Massachusetts Institute of Technology (2018). https://dspace.mit.edu/handle/1721.1/115776.
[7] A. Chernikov, T. Berkelbach, H. Hill, A. Rigosi, Y. Li, O. Aslan, D. Reichman, M. Hybertsen, T. Heinz, Exciton Binding Energy and Nonhydrogenic Rydberg Series in Monolayer WS_2, Phys. Rev. Lett. 113 (2014) 076802, https://doi.org/10.1103/PhysRevLett.113.076802.
[8] M. Cotrufo, L. Sun, J. Choi, A. Alù, X. Li, Enhancing functionalities of atomically thin semiconductors with plasmonic nanostructures, Nanophotonics 8 (2019) 577–598, https://doi.org/10.1515/nanoph-2018-0185.
[9] B. Zheng, Y. Chen, Controllable Growth of Monolayer MoS_2 and $MoSe_2$ Crystals Using Three temperature zone Furnace, IOP Conf. Ser.: Mater. Sci. Eng. 274 (2017) 012085.
[10] M. Sial, M. Usman, A. Moghaddam, A. Channa, Y. Yu, F. Qing, H. Ji, CVD-grown 2D molybdenum diselenide: Morphology, spectroscopic and mechanical characterization, J. Alloys Compd. 803 (2019) 795–803, https://doi.org/10.1016/j.jallcom.2019.06.163.
[11] X. Chen, P. Hu, K. Song, X. Wang, C. Zuo, R. Yang, J. Wang, CVD growth of large-scale hexagon-like shaped $MoSe_2$ monolayers with sawtooth edge, Chem. Phys. Lett. 733 (2019) 136663, https://doi.org/10.1016/j.cplett.2019.136663.
[12] J. Li, W. Yan, Y. Lv, J. Leng, D. Zhang, C. Coileáin, C. Cullen, T. Stimpel-Lindner, G. Duesberg, J. Cho, M. Choi, B. Chun, Y. Zhao, C. Lv, S. Arora, H. Wu, Sub-millimeter size high mobility single crystal $MoSe_2$ monolayers synthesized by NaCl-assisted chemical vapor deposition, RSC Adv. 10 (2020) 1580–1587, https://doi.org/10.1039/C9RA09103C.
[13] Y. Li, F. Wang, D. Tang, J. Wei, Y. Li, Y. Xing, K. Zhang, Controlled synthesis of highly crystalline CVD-derived monolayer $MoSe_2$ and shape evolution mechanism, Mater. Lett. 216 (2018) 261–264, https://doi.org/10.1016/j.matlet.2018.01.102.
[14] Y. Li, K. Zhang, F. Wang, Y. Feng, Y. Li, Y. Han, D. Tang, B. Zhang, Scalable Synthesis of Highly Crystalline $MoSe_2$ and Its Ambipolar Behavior, ACS Appl.

Mater. Interfaces 9 (2017) 36009–36016, https://doi.org/10.1021/acsami.7b10693.
[15] S. Kang, H. Lee, Study on Growth Parameters for Monolayer MoS_2 Synthesized by CVD Using Solution-based Metal Precursors, Appl. Sci. Converg. Technol. 28 (2019) 159–163, https://doi.org/10.5757/ASCT.2019.28.5.159.
[16] T. Dai, Y. Liu, X. Fan, X. Liu, D. Xie, Y. Li, Synthesis of few-layer 2H-MoSe2 thin films with wafer-level homogeneity for high-performance photodetector, Nanophotonics 7 (2018) 1959–1969, https://doi.org/10.1515/nanoph-2018-0153.
[17] J. Xia, X. Huang, L. Liu, M. Wang, L. Wang, B. Huang, D. Zhu, J. Li, C. Gu, X. Meng, CVD synthesis of large-area, highly crystalline $MoSe_2$ atomic layers on diverse substrates and application to photodetectors, Nanoscale 6 (2014) 8949–8955, https://doi.org/10.1039/C4NR02311K.
[18] J.P.B. Silva, C.A. Marques, A.S. Viana, L.F. Santos, K. Gwozdz, E. Popko, J. P. Connolly, K. Veltruská, V. Matolín, O. Conde, Morphological, optical and photovoltaic characteristics of $MoSe_2/SiO_x$/Si heterojunctions, Sci. Rep. 10 (2020) 1215, https://doi.org/10.1038/s41598-020-58164-7.
[19] J. Wei, M. Zhou, A. Long, Y. Xue, H. Liao, C. Wei, Z. Xu, Heterostructured Electrocatalysts for Hydrogen Evolution Reaction Under Alkaline Conditions, Nano Micro Lett. 10 (2018) 75, https://doi.org/10.1007/s40820-018-0229-x.
[20] J. Huang, H. Liu, B.o. Jin, M. Liu, Q. Zhang, L. Luo, S. Chu, S. Chu, R. Peng, Large-area snow-like $MoSe_2$ monolayers: synthesis, growth mechanism, and efficient electrocatalyst application, Nanotechnology 28 (27) (2017) 275704.
[21] J.P.B. Silva, C.A. Marques, J.A. Moreira, O. Conde, Resistive switching in $MoSe_2$/$BaTiO_3$ hybrid structures, J. Mater. Chem. C 5 (2017) 10353–10359, https://doi.org/10.1039/C7TC03024J.
[22] Z.-D. Luo, M.-M. Yang, Y. Liu, M. Alexe, Emerging Opportunities for 2D Semiconductor/Ferroelectric Transistor-Structure Devices, Adv. Mater. 33 (2021) 2005620, https://doi.org/10.1002/adma.202005620.
[23] C. Almeida Marques, Growth and characterization of low dimensional Mo selenide, MSc Thesis, University of Lisbon, (2016). http://hdl.handle.net/10451/25252 (2016).
[24] R.F. Frindt, Single Crystals of MoS_2 Several Molecular Layers Thick, J. Appl. Phys. 37 (1966) 1928–1929, https://doi.org/10.1063/1.1708627.
[25] E. Grayfer, M. Kozlova, V. Fedorov, Colloidal 2D nanosheets of MoS_2 and other transition metal dichalcogenides through liquid-phase exfoliation, Adv. Colloid Interface Sci. 245 (2017) 40–61, https://doi.org/10.1016/j.cis.2017.04.014.
[26] A. Rajan, K. Underwood, F. Mazzola, P. King, Morphology Control of Epitaxial Monolayer Transition Metal Dichalcogenides, Phys. Rev. Mater. 4 (2020), 014003, https://doi.org/10.1103/PhysRevMaterials.4.014003.
[27] D. Zhou, J. Lang, N. Yoo, R. Unocic, Q. Wu, B. Li, Fluid-Guided CVD Growth for Large-Scale Monolayer Two-Dimensional Materials, ACS Appl. Mater. Interfaces 12 (2020) 26342–26349, https://doi.org/10.1021/acsami.0c04125.
[28] J. Zhang, F. Wang, V. Shenoy, M. Tang, J. Lou, Towards controlled synthesis of 2D crystals by chemical vapor deposition (CVD), Mater. Today 40 (2020) 132–139, https://doi.org/10.1016/j.mattod.2020.06.012.
[29] G. Peng, X. Yang, S. Wang, J. Zhang, G. Qi, S. Zhang, K. Liu, Z. Zhu, Z. Li, G. Wang, M. Zhu, S. Qin, Controllable Epitaxial Growth of $MoSe_2$ Bilayers with Different Stacking Orders by Reverse-flow Chemical Vapor Deposition, ACS Appl. Mater. Interfaces 12 (2020) 23347–23355, https://doi.org/10.1021/acsami.0c04411.
[30] L. Meng, S. Hu, W. Yan, J. Feng, H. Li, X. Yan, Controlled Synthesis of Large Scale Continuous monolayer WS_2 Film by Atmospheric Pressure Chemical Vapor Deposition, Chem. Phys. Lett. 739 (2019) 136945, https://doi.org/10.1016/j.cplett.2019.136945.
[31] Z. Wang, H. Yang, S. Zhang, J. Wang, K. Cao, Y. Lu, W. Hou, S. Guo, X.-A. Zhang, L. i. Wang, An approach to high-throughput growth of submillimeter transition metal dichalcogenide single crystals, Nanoscale 11 (46) (2019) 22440–22445.
[32] S. Chowdhury, A. Roy, I. Bodemann, S. Banerjee, Two-Dimensional to Three-Dimensional Growth of Transition Metal Diselenides by Chemical Vapor Deposition: Interplay between Fractal, Dendritic and Compact Morphologies, ACS Appl. Mater. Interfaces 12 (2020) 15885–15892, https://doi.org/10.1021/acsami.9b23286.
[33] S. Wang, Y. Rong, Y. Fan, M. Pacios, H. Bhaskaran, K. He, J. Warner, Shape Evolution of Monolayer MoS2 Crystals Grown by Chemical Vapor Deposition, Chem. Mater. 26 (2014) 6371–6379, https://doi.org/10.1021/cm5025662.
[34] U. Gupta, C.N.R. Rao, Hydrogen generation by water splitting using MoS2 and other transition metal dichalcogenides, Nano Energy 41 (2017) 49–65, https://doi.org/10.1016/j.nanoen.2017.08.021.
[35] C. González, Nanoestruturas bidimensionais de $MoSe_2$: de triângulos a fractais, MSc Thesis, University of Lisbon, (2021). https://repositorio.ul.pt/handle/10451/50782.
[36] H. Bergeron, V.K. Sangwan, J.J. McMorrow, G.P. Campbell, I. Balla, X. Liu, M. J. Bedzyk, T.J. Marks, M.C. Hersam, Chemical Vapor Deposition of Monolayer MoS2 Directly on Ultrathin Al_2O_3 for Low-Power Electronics, Appl. Phys. Lett. 110 (5) (2017) 053101.
[37] Y. Zhang, Y. Zhang, Q. Ji, J. Ju, H. Yuan, J. Shi, T. Gao, D. Ma, M. Liu, Y. Chen, X. Song, H. Hwang, Y. Cui, Z. Liu, Controlled Growth of High-Quality Monolayer WS_2 Layers on Sapphire and Imaging Its Grain Boundary, ACS Nano 7 (2013) 8963–8971, https://doi.org/10.1021/nn403454e.
[38] P. Yang, X. Zou, Z. Zhang, M. Hong, J. Shi, S. Chen, J. Shu, L. Zhao, S. Jiang, X. Zhou, Y. Huan, C. Xie, P. Gao, Q. Chen, Q. Zhang, Z. Liu, Y. Zhang, Batch production of 6-inch uniform monolayer molybdenum disulfide catalyzed by sodium in glass, Nat. Commun. 9 (2018) 979, https://doi.org/10.1038/s41467-018-03388-5.
[39] J. Chen, X. Zhao, S. Tan, H. Xu, B. Wu, B. Liu, D. Fu, W. Fu, D. Geng, Y. Liu, W. Liu, W. Tang, L. Linjun, W. Zhou, T. Sum, K. Loh, Chemical Vapor Deposition of Large-Size Monolayer $MoSe_2$ Crystals on Molten Glass, J. Am. Chem. Soc. 139 (2017) 1073–1076, https://doi.org/10.1021/jacs.6b12156.
[40] H. Wang, D. Zhu, F. Jiang, P. Zhao, H. Wang, Z.e. Zhang, X. Chen, C. Jin, Revealing the microscopic CVD growth mechanism of $MoSe_2$ and the role of hydrogen gas during the growth procedure, Nanotechnology 29 (31) (2018) 314001.
[41] V. Singh, D. Late, A. Goyal, S. Rath, Raman spectroscopic investigations of the selenization of MoO_3 in the chemical vapor deposition process to form two-dimensional $MoSe_2$, Appl. Surface Sci. 538 (2021) 147946, https://doi.org/10.1016/j.apsusc.2020.147946.
[42] M. Dieterle, G. Mestl, Raman spectroscopy of molybdenum oxides Part II. Resonance Raman spectroscopic characterization of the molybdenum oxides Mo_4O_{11} and MoO_2, Phys. Chem. Chem. Phys. 4 (2002) 822–826, https://doi.org/10.1039/B107046K.
[43] T. Chen, G. Hao, G. Wang, B. Li, L. Kou, H. Yang, X. Zheng, J. Zhong, Controlled growth of atomically thin $MoSe_2$ films and nanoribbons by chemical vapor deposition, 2D Mater. 6 (2019) 025002, https://doi.org/10.1088/2053-1583/aaf9cc.
[44] X. Li, M.-W. Lin, A.A. Puretzky, J.C. Idrobo, C. Ma, M. Chi, M. Yoon, C.M. Rouleau, I.I. Kravchenko, D.B. Geohegan, K. Xiao, Controlled Vapor Phase Growth of Single Crystalline, Two-Dimensional GaSe Crystals with High Photoresponse, Sci. Rep. 4 (2014) 5497, https://doi.org/10.1038/srep05497.
[45] S. Cui, B. Hu, B. Ouyang, D. Zhao, Thermodynamic assessment of the Mo-S system and its application in thermal decomposition of MoS_2, Thermochim. Acta 660 (2018) 44–55, https://doi.org/10.1016/j.tca.2017.12.011.
[46] D. Zhou, H. Shu, C. Hu, L. Jiang, P. Liang, X. Chen, Unveiling the Growth Mechanism of MoS_2 with Chemical Vapor Deposition: From Two-Dimensional Planar Nucleation to Self-Seeding Nucleation, Cryst. Growth Des. 18 (2018) 1012–1019, https://doi.org/10.1021/acs.cgd.7b01486.
[47] D. Zhou, H. Shu, F. Jiang, D. Lv, V. Asokan, O. Omar, J. Yuan, Z. Zhang, C. Jin, Capture the growth kinetics of CVD growth of two-dimensional MoS_2, npj 2D Mater. Appl. 1 (2017) 8, https://doi.org/10.1038/s41699-017-0010-x.
[48] P. Wang, S. Luo, L. Boyle, H. Zeng, S. Huang, Controlled fractal growth of transition metal dichalcogenides, Nanoscale 11 (2019) 17065–17072, https://doi.org/10.1039/C9NR06358G.
[49] T.A. Witten, L.M. Sander, Diffusion-limited aggregation, a kinetic critical phenomenon, Phys. Rev. Lett. 47 (1981) 1400–1403, https://doi.org/10.1103/PhysRevLett.47.1400.
[50] K.J. Falconer, Fractal Geometry: Mathematical Foundations and Applications, Wiley, Chichester, 2003.
[51] S. Morris, Box counting algorithm for estimating fractal dimension of a binarized image. https://www.physics.utoronto.ca/~phy326/fvf/python_code/box_count.py/, 2017 (accessed 29 January 2021).
[52] J.C. Shaw, H. Zhou, Y. Chen, N.O. Weiss, Y. Liu, Y. Huang, X. Duan, Chemical vapor deposition growth of monolayer MoSe2 nanosheets, Nano Res. 7 (2014) 511–517, https://doi.org/10.1007/s12274-014-0417-z.
[53] S. Tongay, J. Zhou, C. Ataca, K. Lo, T.S. Matthews, J. Li, J.C. Grossman, J. Wu, Thermally driven crossover from indirect toward direct bandgap in 2d semiconductors: MoSe2 versus MoS2, Nano Lett. 12 (2012) 5576–5580, https://doi.org/10.1021/nl302584w.
[54] G.W. Shim, K. Yoo, S. Seo, J. Shin, D.Y. Jung, I. Kang, C.W. Ahn, B.J. Cho, S. Choi, Large-area single-layer MoSe2 and its van der waals heterostructures, ACS Nano 8 (2014) 6655–6662, https://doi.org/10.1021/nn405685j.
[55] V.S. Minaev, S.P. Timoshenkov, V.V. Kalugin, Structural and phase transformations in condensed selenium, J. Optoelectron. Adv. Mater. 7 (2005) 1717–1741.
[56] A.O.A. Tanoh, J. Alexander-Webber, Y.e. Fan, N. Gauriot, J. Xiao, R. Pandya, Z. Li, S. Hofmann, A. Rao, Giant photoluminescence enhancement in MoSe2 monolayers treated with oleic acid ligands, Nanoscale Adv. 3 (14) (2021) 4216–4225.
[57] M. Cowie, R. Plougmann, Y. Benkirane, L. Schué, Z. Schumacher, P. Grütter, How high is a $MoSe_2$ monolayer? Nanotechnology 33 (12) (2022) 125706.
[58] K.M. McCreary, A.T. Hanbicki, S.V. Sivaram, B.T. Jonker, A- and B-exciton photoluminescence intensity ratio as a measure of sample quality for transition metal dichalcogenide monolayers, APL Mater. 6 (11) (2018) 111106.
[59] F. Chen, Q. Lv, Y. Xia, S. Mao, Y. Li, Controllable Synthesis of Large-Scale Monolayer MoS2 Dendritic Flakes with Serrated Edges and Their Multimodal Microscopy and AFM Characterizations, J. Phys. Chem. C (2022), https://doi.org/10.1021/acs.jpcc.2c03609.